Optica Applicata, Vol. LIV, No. 3, 2024
DOI: 10.37190/oa240307

Aerial infrared small target detection algorithm combined structure tensor and local contrast

Zhonghua Wang[1,*], Bangsheng He[2], Wenjie He[3]

[1] School of Information Engineering, Nanchang Hangkong University,
Nanchang 330063, China

[2] School of Information Engineering, Nanchang Hangkong University,
Nanchang 330063, China

[3] School of Information Engineering, Nanchang Hangkong University,
Nanchang 330063, China

[*] Corresponding author: wangzhonghua@nchu.edu.cn

To solve the problem of false alarm rate in detecting infrared small targets under complex cloud backgrounds, a novel algorithm combining structure tensor and local contrast is proposed. The structure tensor can better describe the gradient distributions in the local image area, and its eigenvalues can also depict the characteristics of the area. Combining the weighted local contrast with eigenvalues, the small targets can be enhanced and the background can be suppressed. In addition, to highlight the target, the regional complexity is further used for weighting local contrast. The presented algorithm steps are as follows: firstly, Gaussian filtering is performed on the original image; secondly, the larger eigenvalue of the structure tensor matrix is used to calculate the local contrast through the difference operation; thirdly, the regional complexity is calculated by the gray difference between the central and surrounding regions for weighting the local contrast to generate a saliency map; finally, an adaptive threshold segmentation is performed on the saliency map to extract the real target. The comparative experiments show that the proposed algorithm can achieve the highest detection rate, lowest false alarm rate, and shortest running time.

Keywords: adaptive threshold segmentation, local contrast, regional complexity, small target, structure tensor.

1. Introduction

With the development of science and technology, the application of infrared detection systems has been paid more and more attention [1]. Compared with other detection technologies, infrared imaging detection technology has the advantages of long detection distance, high concealment, strong anti-interference ability, *etc*. [2]. Therefore, it is widely used in military and civilian fields [3] such as precision guidance, early warning, and maritime search and rescue [4].

Usually, the small target in the air is far away from the infrared imaging equipment, resulting in fewer imaging pixels [5], and the imaging target has no specific structure and texture information [6, 7]. In addition, the small target is easily submerged in complex backgrounds and strong noises [8]. Therefore, it remains a challenge to detect infrared small targets in long-distance air accurately [9, 10].

Traditional methods such as wavelet transformation [11], morphological top-hat filtering [12], and max-mean and max-median filtering [13] have good performance in detecting small targets in simple air backgrounds [14]. However, those methods tend to generate a large false alarm rate under complex air backgrounds [15].

In recent years, bionic methods based on human visual attention mechanisms have attracted the attention of many researchers [16]. Human eyes not only depend on the gray value of the target but rely more on the contrast between the target and its surrounding backgrounds to recognize the target accurately [17, 18]. Hence, the contrast mechanism has been introduced by many researchers in the field of infrared small target detection [19, 20].

According to the contrast mechanism based on human visuals, CHEN *et al.* [21] proposed LCM, which detected the small target by calculating the maximum contrast between the target and its surrounding areas at multiple scales. ZHANG *et al.* [22] proposed ILCM, which calculated the local contrast with the difference operation to suppress continuous background. DU *et al.* [23] proposed HWLCM, which used the local contrast and homogeneity features to detect the small target. HAN *et al.* [24] proposed WSLCM, which is based on the weighted strengthened local contrast measure. That is to say, by calculating the difference between each pixel region and its surrounding area, the weak targets are highlighted and the background is suppressed.

However, the algorithms proposed by CHEN, ZHANG, and DU are sensitive to strong background edges and easy to generate a high false alarm rate. Han's algorithm can effectively suppress strong background edges, but its detection time is too long. Compared with the traditional algorithms, the detection performance of the algorithm based on the contrast mechanism has improved to some extent [25]. However, there are still problems that the background edge may be falsely detected as the target [26, 27] and the detection time is long [28] when detecting small targets under complex backgrounds. There is still room for improving the detection performance of the existing local contrast algorithm in complex backgrounds.

Recently researchers have begun to incorporate new theories into local contrast algorithms, such as high-boost-based multiscale local contrast measure [29], multiscale local contrast measure using local energy factor [30], and the Gaussian scale-space enhanced local contrast measure [31]. However, these algorithms did not consider the gradient difference between the target and background. As is well known, the gradient distribution of small target is different from its neighboring background. Depicting the gradient distribution of the local image area, the structural tensor is used to distinguish the small targets from the background. Therefore, this paper proposes an infrared small target detection algorithm that combines structure tensor and local contrast. The proposed algorithm can effectively improve the detection rate, reduce the false alarm rate, and shorten the detection time.

2. Related works

In the field of image processing, the structure tensor is usually applied in corner detection. It is defined as

$$J = D_\alpha * (\nabla G_\beta \otimes \nabla G_\beta) = \begin{bmatrix} D_\alpha * (V_x^2) & D_\alpha * (V_x V_y) \\ D_\alpha * (V_y V_x) & D_\alpha * (V_y^2) \end{bmatrix} = \begin{bmatrix} J_{11} & J_{12} \\ J_{21} & J_{22} \end{bmatrix} \tag{1}$$

where D_α is the Gaussian kernel function with variance α, G_β represents the original image G filtered by Gaussian filter with variance β, $*$ is convolution operation, ∇ is the gradient, $\otimes$ is the outer product. V_x is horizontal gradient, $V_x = \partial G_\beta / \partial x$; V_y is vertical gradient, $V_y = \partial G_\beta / \partial y$. J is the structure tensor, J_{11}, J_{12}, J_{21} and J_{22} are the four elements of J. The two eigenvalues of J are denoted as λ_a and λ_b, which can be obtained via

$$\begin{cases} \lambda_a = (J_{11} + J_{22}) + \sqrt{(J_{22} - J_{11})^2 + 4 J_{12}^4} \\ \lambda_b = (J_{11} + J_{22}) - \sqrt{(J_{22} - J_{11})^2 + 4 J_{12}^4} \end{cases} \tag{2}$$

The features of the local image area can be reflected through the two eigenvalues: for the corner region, $\lambda_a \geq \lambda_b \gg 0$; for the edge region, $\lambda_a \gg \lambda_b \approx 0$; for the flat region, $\lambda_a \approx \lambda_b \approx 0$.

The gradients of a small target are large in all directions in the local image area, which is similar to the corner point. So we consider applying a structure tensor to help detect the small target. But, different from the corner point, the small target is approximately circular and occupies a few pixels, which owns a small spatial range. Therefore, we cannot directly use the original structure tensor to describe the gradient features of the small target. Given the local saliency of the small target, the paper proposes a new gradient calculation method that combines the idea of local contrast, which will be discussed in the next section.

3. Proposed method

The proposed algorithm mainly includes three parts: Gaussian filtering preprocessing, saliency map generation and adaptive threshold segmentation. Figure 1 shows the flowchart of the algorithm proposed in this paper. The small target is marked by the red rectangle and the backgrounds and noises are marked by the blue ovals.

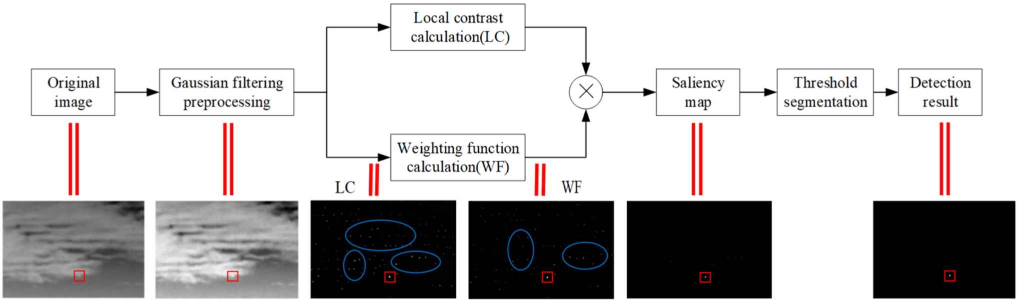

Fig. 1. Flowchart of the proposed algorithm.

3.1. Gaussian filtering preprocessing

The original infrared image is usually composed of the real target, pixel-sized noise with high brightness (PNHB), background edges, and flat backgrounds. The PNHB in the original infrared image is easy to be misdetected as targets. So, it is necessary to suppress the PNHB before generating the saliency map. According to the theory of matched filter [32], when the shape of the filter is similar to that of the small target, it can keep the characteristics of the small target. Since the gray distribution of the target is consistent with the Gaussian distribution, Gaussian filtering is used to process the original infrared image in this paper. Since the size of the target is smaller than 3×3 in this paper, the size of the Gaussian filter is defined as 3×3 and its template is shown in Fig. 2.

$\frac{1}{16}$	$\frac{1}{8}$	$\frac{1}{16}$
$\frac{1}{8}$	$\frac{1}{4}$	$\frac{1}{8}$
$\frac{1}{16}$	$\frac{1}{8}$	$\frac{1}{16}$

Fig. 2. 3×3 Gaussian filter template.

3.2. Saliency map generation

3.2.1. Construction of structure tensor matrix

The proposed algorithm combines the idea of local contrast to construct the structure tensor matrix with the gray difference between the central cell and the surrounding cells. Compared with the original structure tensor containing the horizontal, vertical, and diagonal gradients in the local image area, the proposed tensor matrix can better characterize the gradient distribution of the local image area.

To obtain the computational area of the structure tensor, a moving window is designed to traverse the image. As the window moves, different image patches such as

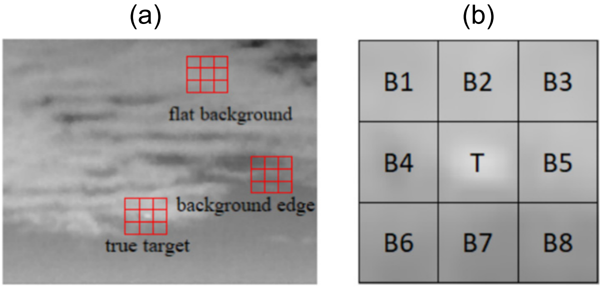

Fig. 3. (a) Moving window captures different image patches. (b) Enlarged moving window.

flat backgrounds, background edges, and the real target are captured, as shown in Fig. 3(a). The size of the moving window is set to be 9 × 9, and it is divided into 9 cells. The enlarged moving window is shown in Fig. 3(b). The central cell T is used to capture the target, and the surrounding 8 cells B1–B8 are used to capture the background.

For each cell, like WSLCM, the mean of the K maximal gray values is calculated. m_0 denotes the mean of the K maximal gray values of the central cell and m_1–m_8 respectively denote the mean of the K maximal gray values of the corresponding surrounding cells. They are calculated through (3) and (4), respectively.

$$m_0 = \frac{1}{K}\sum_{j=1}^{K} T_j \tag{3}$$

$$m_i = \frac{1}{K}\sum_{j=1}^{K} B_j^i, \qquad i = 1, 2, ..., 8 \tag{4}$$

where T_j represents the j-th maximal gray value of the cell T and B_j^i represents the j-th maximal gray value of the i-th surrounding a cell.

According to the definition of the Society of Photo-Optical Instrumentation Engineers (SPIE), the size of the small target is less than 9 × 9 [33]. The size of the small target in the infrared image sequences used in this paper ranges from 2 × 2 to 3 × 3, so the proposed algorithm is mainly applied to detect small targets in the range of 2 × 2 to 3 × 3. Referring to WSLCM, the value of K is set to be 4. Then, one image sequence is selected for the experiment, and the result is shown in Fig. 4. It can be seen from Fig. 4 that the proposed algorithm achieves the best detection effect when K is set to 4. Meanwhile, the computational complexity of the algorithm is also minimal while K is 4.

For constructing the structure tensor matrix, the surrounding cells B1–B8 are divided into four regions in four directions. The horizontal, vertical, and two diagonal directions are defined as the XX, YY, XY, and YX directions, respectively. The specific definition is given in Fig. 5.

There are two surrounding cells in each direction where m_i and m_{9-i} ($i = 1, 2, 3, 4$) are used to make a difference with M_0, respectively, the smaller difference value is de-

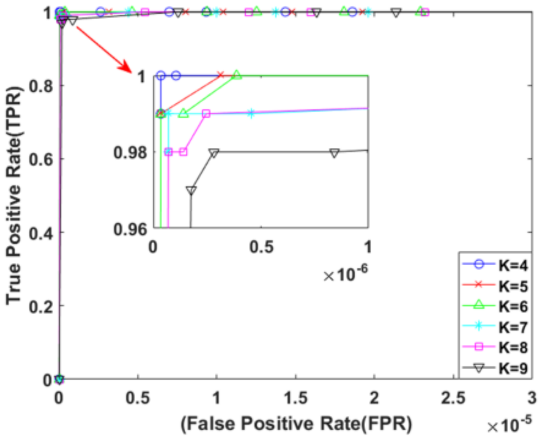

Fig. 4. ROC curves of different parameters *K*.

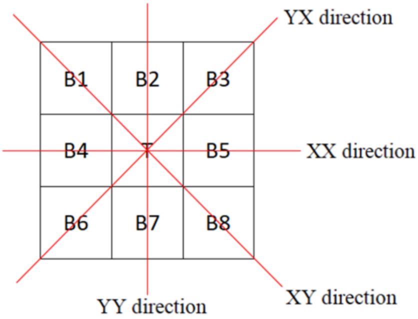

Fig. 5. Direction definition.

fined as the gradient value of horizontal, vertical, or diagonal directions. The M_0 and structure tensor matrix ST are defined as follows:

$$M_0 = m_0 \times \left(\min \frac{m_0}{m_i}\right), \qquad i = 1, 2, ..., 8 \tag{5}$$

$$\mathrm{ST}_{XX} = \min(M_0 - m_4, M_0 - m_5) \tag{6}$$

$$\mathrm{ST}_{YY} = \min(M_0 - m_2, M_0 - m_7) \tag{7}$$

$$\mathrm{ST}_{XY} = \min(M_0 - m_1, M_0 - m_8) \tag{8}$$

$$\mathrm{ST}_{YX} = \min(M_0 - m_3, M_0 - m_6) \tag{9}$$

$$\mathrm{ST} = \begin{bmatrix} \mathrm{ST}_{XX} & \mathrm{ST}_{XY} \\ \mathrm{ST}_{YX} & \mathrm{ST}_{YY} \end{bmatrix} \tag{10}$$

Where ST_{XX}, ST_{YY}, ST_{XY}, and ST_{YX} are the gradient values of the four directions, respectively.

3.2.2. Calculation of local contrast

The proposed algorithm utilizes the larger eigenvalue of the structure tensor to calculate the local contrast instead of the commonly used ratio difference formula. The larger eigenvalues obtained from different image areas are different in values. Therefore, the eigenvalue decomposition operation is performed on ST, and the obtained two eigenvalues are recorded as λ_1 and λ_2. Then, the calculation of local contrast is defined in (12).

$$E(x, y) = \max(\lambda_1, \lambda_2) \tag{11}$$

$$\mathrm{LC}(x, y) = E(x, y) \times G(x, y) - G(x, y) \tag{12}$$

where (x, y) is the current pixel coordinate, $E(x, y)$ is the gain coefficient of the current pixel, $G(x, y)$ is the gray value of the current pixel in the original image, and $\mathrm{LC}(x, y)$ is the local contrast of the current pixel.

The larger the four elements of ST, the larger the obtained eigenvalues. On the contrary, the smaller the four elements of ST, the smaller the obtained eigenvalues. The ST, λ_1, and λ_2 of different image areas are shown in Table 1. The red rectangle areas are the calculation regions of ST. It can be seen from Table 1 that the larger eigenvalue of the target area is much bigger than those of the background edge, flat background, and PNHB. Therefore, compared with other background areas, the target is significantly enhanced. As shown in Fig. 6, the target is much more prominent in the local contrast map than in the noise image.

Table 1. ST, λ_1, and λ_2 of different image areas.

Different image areas	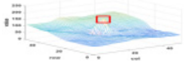 Target area	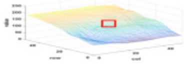 Background edge	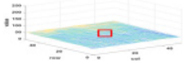 Flat background	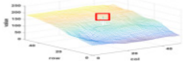 PNHB
ST	$\begin{bmatrix} 70.20 & 98.98 \\ 78.29 & 50.92 \end{bmatrix}$	$\begin{bmatrix} -19.96 & -28.77 \\ -20.07 & -24.19 \end{bmatrix}$	$\begin{bmatrix} -3.76 & -3.87 \\ -3.78 & -3.52 \end{bmatrix}$	$\begin{bmatrix} -4.55 & -13.37 \\ -4.66 & -8.78 \end{bmatrix}$
λ_1	149.12	2.05	0.19	1.51
λ_2	–28.00	–46.20	–7.47	–14.84

3.2.3. Calculation of weight and saliency

To further highlight the target, the regional complexity of the local image area is introduced to weight the local contrast. The regional complexity weight and saliency are respectively defined as:

$$\mathrm{WF}(x, y) = \max\{\min(m_0 - m_i), 0\}, \quad i = 1, 2, ..., 8 \tag{13}$$

$$S(x, y) = \mathrm{LC}(x, y) \times \mathrm{WF}(x, y) \tag{14}$$

Where $\mathrm{WF}(x, y)$ and $S(x, y)$ are the regional complexity weight and saliency of the current pixel respectively.

For the target area, $m_0 > m_i$, the regional complexity weight of the target is large. For the background edge area, $m_0 \leq m_i$, its regional complexity weight is small. For the flat background and PNHB, m_0 and m_i are close, thus their regional complexity weights are small.

The target region is cropped for experiments to prove the effectiveness of the local contrast and weighting calculation. The experimental results are shown in Fig. 6.

Where Fig. 6(a)−(d) are the 3D normalized value distribution maps of the cropped original image, the noise image which is the original image adding PNHB, the local contrast map, and the saliency map, respectively. Compared with the local contrast map, the target is enhanced again while the background edges and PNHB are suppressed again in the saliency map. Therefore, the regional complexity can further highlight the target.

The central pixel of the moving window is replaced by the calculated saliency in this paper. After the moving window traverses the image, the saliency map of the original image can be obtained.

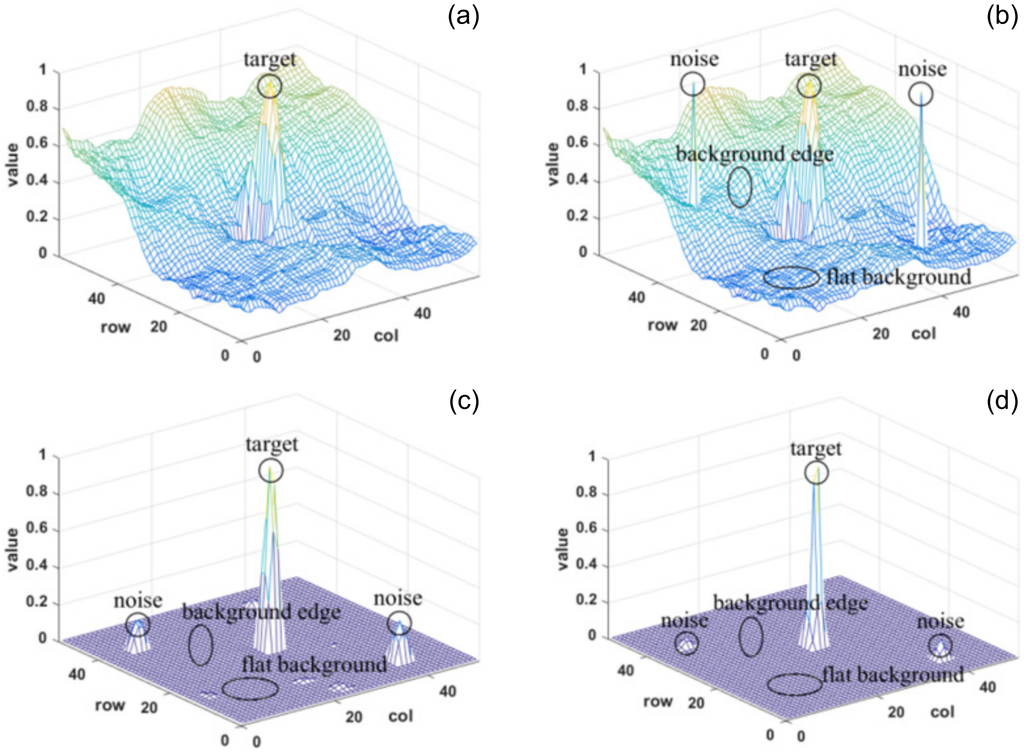

Fig. 6. (a)-(d) 3D normalized value distribution maps of the cropped original image, the noise image which is the original image adding PNHB, the local contrast map, and the saliency map, respectively.

3.3. Threshold segmentation

In the saliency map, pixels with larger values are more likely to be the target. Adaptive threshold segmentation is performed on the saliency map to extract the target. The threshold is defined as

$$\mathrm{Th} = \frac{k \times \mathrm{Max} + \mathrm{Min}}{k+1} \tag{15}$$

where Max and Min are the maximum and minimum values of the saliency map respectively, k is an adjustment parameter, generally ranging from 1 to 3. The pixels in the saliency map that are greater than the threshold Th are considered as the target, otherwise they are considered as the background.

4. Experimental results

To verify the background suppression performance and target detection performance of the proposed algorithm, three real infrared image sequences with different cloud backgrounds are selected for experiments. The feature descriptions of different sequence images are as follows. The characteristics of the first sequence of images are low-speed weak aerial targets and altocumulus layers. The characteristics of the second sequence of images are low-speed small aerial targets and stratocumulus layers. The characteristics of the third sequence of images are high-speed small aerial targets and altostratus layers. Table 2 presents the details of the three image sequences. To prove the superiority of the proposed algorithm, it will be compared with several other algorithms including LCM, ILCM, TLWLCM [34], HWLCM, SWLCM [35], and WSLCM.

Table 2. Detail of sequence images.

Sequence	Resolution	Frame	Target description	Background description
Seq.1	460×620	100	Dim, low contrast, slow-moving airplane	Altocumulus, slowly changing clouds
Seq.2	460×620	90	Small, low contrast, slow-moving airplane	Stratocumulus, violently changing clouds
Seq.3	460×620	100	Small, higher contrast, fast-moving airplane	Altostratus, smooth clouds

All the experimental procedures in this paper run on a laptop with a 2.6 GHz Intel Core i7-6700HQ processor and 8G memory, and the programming software is MATLAB R2016a.

4.1. Background suppression performance

To verify the background suppression ability of the proposed algorithm, one frame image is randomly selected from each sequence for testing. Figure 7 shows the three orig-

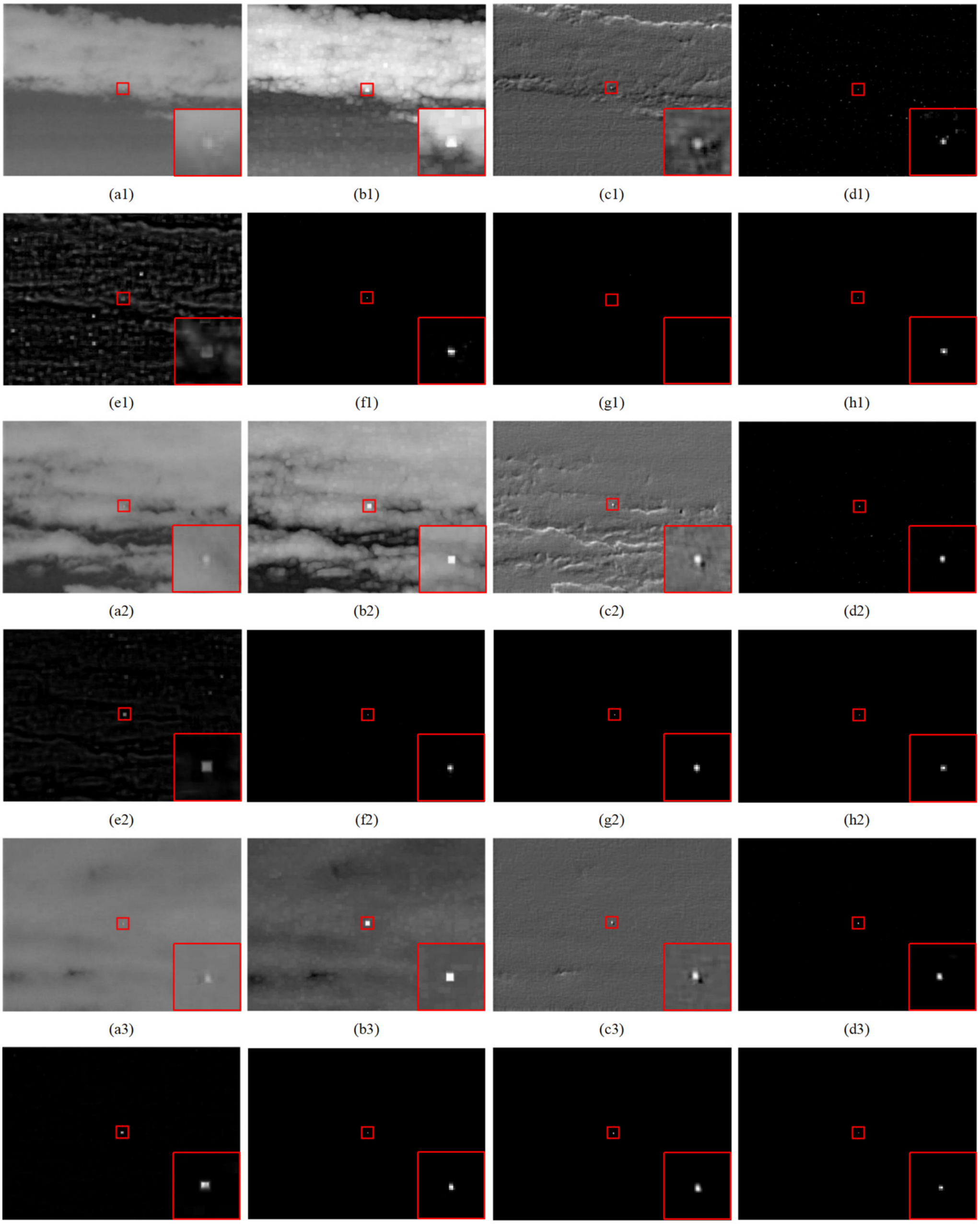

(a1) (b1) (c1) (d1)

(e1) (f1) (g1) (h1)

(a2) (b2) (c2) (d2)

(e2) (f2) (g2) (h2)

(a3) (b3) (c3) (d3)

(e3) (f3) (g3) (h3)

Fig. 7. (a1)–(a3) Original images in sequences 1–3. (b1)–(b3) to (h1)–(h3) Saliency maps obtained by LCM, ILCM, TLWLCM, HWLCM, SWLCM, WSLCM, and the proposed algorithm, respectively. The target areas are marked by red rectangles, and the enlarged target areas are in the lower right corner.

inal infrared images and the corresponding saliency maps obtained by different algorithms. In Fig. 7, the target areas are marked by red rectangles, and the enlarged target areas are in the lower right corner. Figure 7(a1)–(a3) are the original images selected from sequences 1 to 3 which respectively correspond to scenes 1 to 3.

LCM and ILCM have the worst performance, many continuous backgrounds are left in their saliency maps. The performance of HWLCM is better than the above-mentioned two algorithms, but it also cannot completely remove the backgrounds. There are still a lot of isolated backgrounds and a few background edges in the saliency map. TLWLCM and WSLCM perform well in the latter two scenes, but a few isolated strong backgrounds are left in their saliency map of the first scene. Although SWLCM and the proposed algorithm perform well in the three scenes, the target is more obvious in the saliency map obtained by the proposed algorithm in the first scene.

To compare the target enhancement and background suppression capabilities of different algorithms more quantitatively, signal-to-clutter ratio gain (SCRG) and background suppression factor (BSF) are introduced to evaluate the performance of these algorithms [36] which are respectively defined as:

$$\mathrm{SCRG} = \frac{\mathrm{SCR_{out}}}{\mathrm{SCR_{in}}} \tag{16}$$

$$\mathrm{SCR} = \frac{|I_\mathrm{t} - \mu_\mathrm{b}|}{\sigma_\mathrm{b}} \tag{17}$$

$$\mathrm{BSF} = \frac{\sigma_\mathrm{in}}{\sigma_\mathrm{out}} \tag{18}$$

Figure 8 shows the 3D normalized value distribution maps of the original infrared images and the processed images obtained by different algorithms. In Fig. 8, the real targets are marked by red rectangles. In the 3D maps obtained by LCM, ILCM, TLWLCM, HWLCM, SWLCM, WSLCM and the proposed algorithm, the background suppression ability of the former four algorithms is relatively weaker. WSLCM has a good background suppression effect in the latter two scenes. But in the first scene, WSLCM mistakenly suppresses the real target. Though SWLCM and the proposed algorithm can accurately enhance the targets and suppress the backgrounds in three scenes, the proposed algorithm can better highlight the target in the first scene. In short, compared with other algorithms, the proposed algorithm can improve the saliency of the targets in different scenes more effectively.

Where $\mathrm{SCR_{in}}$ and $\mathrm{SCR_{out}}$ are the signal-to-clutter ratios of the original and processed images, respectively. I_t represents the maximum gray value of the target area. μ_b and σ_b respectively represent the mean and standard variance of the background area within a certain range around the target area. SCR is the signal-to-clutter ratio. σ_in and σ_out represent the gray standard deviation of the background area of the image before and after processing, respectively. The larger the SCRG, the better the target enhance-

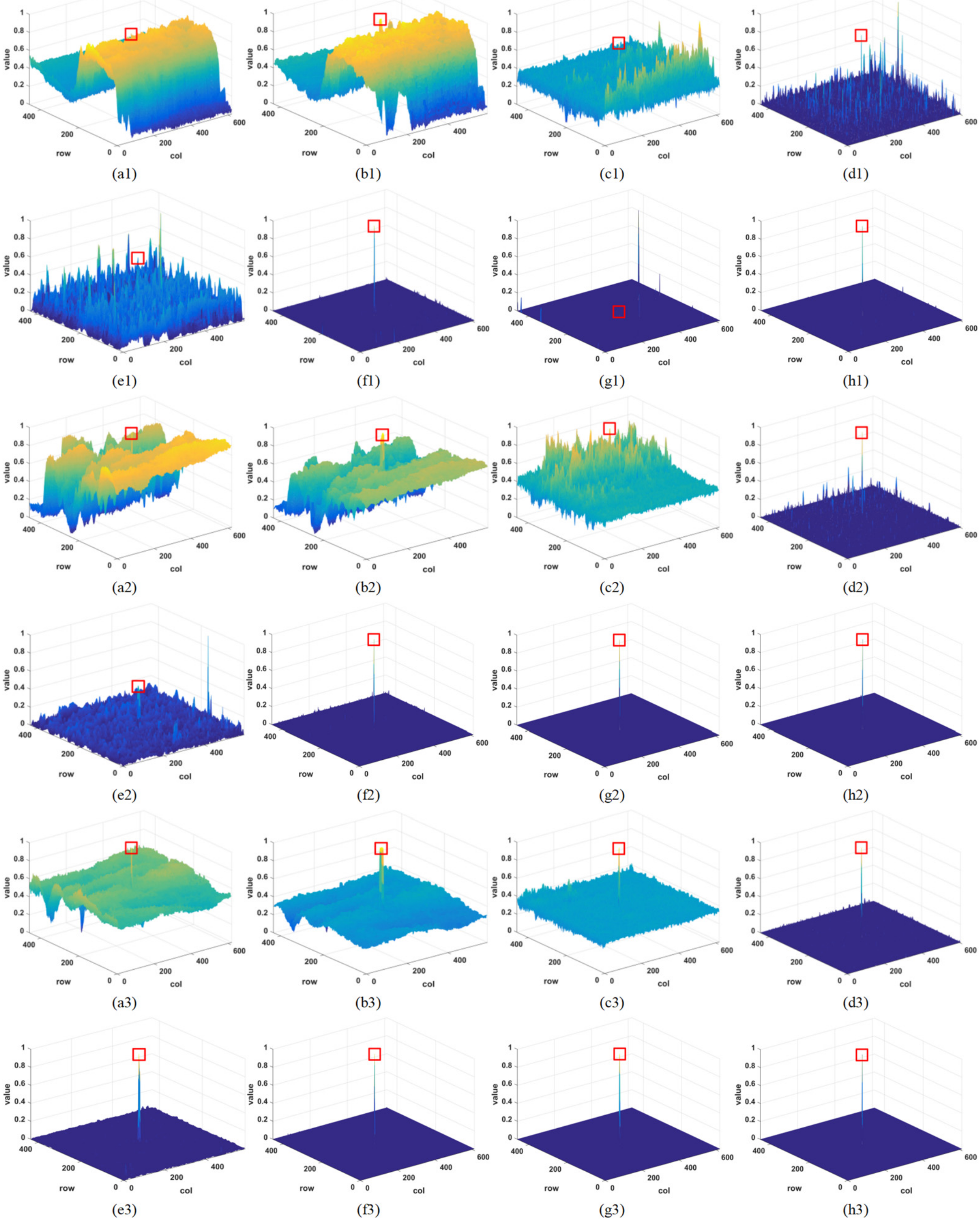

(a1) (b1) (c1) (d1)

(e1) (f1) (g1) (h1)

(a2) (b2) (c2) (d2)

(e2) (f2) (g2) (h2)

(a3) (b3) (c3) (d3)

(e3) (f3) (g3) (h3)

Fig. 8. (a1)–(a3) 3D normalized value distribution maps of original images in sequences 1–3. (b1)–(b3) to (h1)–(h3) 3D normalized value distribution maps obtained by LCM, ILCM, TLWLCM, HWLCM, SWLCM, WSLCM, and the proposed algorithm, respectively. The real targets are marked by red rectangles.

Table 3. SCRG of different algorithms in different scenes.

Scenes	LCM	ILCM	TLWLCM	HWLCM	SWLCM	WSLCM	Proposed
1	1.2288	4.1937	27.3449	2.7374	84.3067	557.5565	987.2341
2	1.0088	1.7875	47.7289	3.6389	130.6821	2197.8355	6529.4346
3	0.19819	0.35097	8.5606	4.8841	67.1514	424.947	595.7712

Table 4. BSF of different algorithms in different scenes.

Scenes	LCM	ILCM	TLWLCM	HWLCM	SWLCM	WSLCM	Proposed
1	0.97261	4.187	10.9222	3.2405	100.1795	51.9729	211.5409
2	1.4438	3.9637	30.2513	8.7662	195.2653	39106.851	865.7083
3	1.4762	2.936	17.9503	14.0249	286.0269	16586.44	762.6519

ment effect of the algorithm. The larger the BSF, the better the background suppression ability of the algorithm.

The SCRG and BSF of different algorithms are shown in Table 3 and Table 4. The SCRG of the proposed algorithm is the largest in all three scenes. The BSF of the proposed algorithm is larger than those of LCM, ILCM, TLWLCM, HWLCM and SWLCM in all scenes. Compared with WSLCM, although the BSF of the proposed algorithm is not the largest in some scenes, they are large enough to distinguish the target from the background. As shown in Fig. 8(h2)–(h3), the value of the target is much bigger than those of the backgrounds and noises.

4.2. Detection performance

To objectively evaluate the detection performance of different algorithms, the receiver operating characteristic (ROC) curve is introduced in this paper [37]. The ROC curve is drawn in a two-dimensional coordinate system where the horizontal and vertical axes are described by the false alarm rate and the detection rate. The detection rate (TPR) and false alarm rate (FPR) are respectively defined by (19) and (20).

$$\mathrm{TPR} = \frac{\text{Number of detected true targets}}{\text{Total number of real targets}} \tag{19}$$

$$\mathrm{FPR} = \frac{\text{Number of detected false targets}}{\text{Total number of pixels in sequence images}} \tag{20}$$

The higher the detection rate and the lower the false alarm rate, the better the detection performance of the algorithm. When the false alarm rate is constant, the higher the detection rate, the better the performance of the algorithm. In the ROC curve, the closer the curve is to the upper left region, the better the performance of the algorithm.

Figure 9 shows the ROC curves obtained by the proposed algorithm and the other six algorithms where Fig. 9(a)–(c) are the ROC curves of sequences 1–3, respectively. In sequence 3, the target has higher contrast while the background has simpler feature,

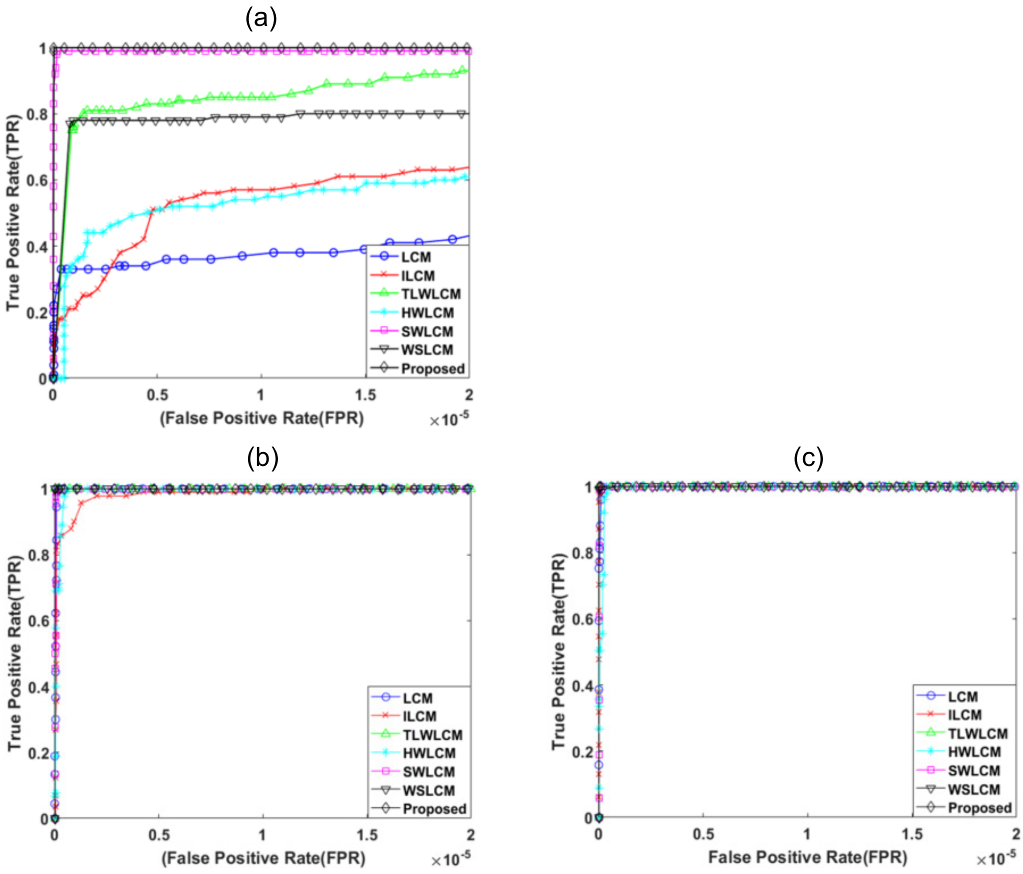

Fig. 9. (a)–(c) ROC curves of different algorithms in sequences 1–3.

so all algorithms can achieve high detection rates. In sequences 1 and 2, although the target has low contrast and the background is more complex, the proposed algorithm can achieve higher detection rates compared with other algorithms. In general, the target detection performance of the proposed algorithm is better than that of other algorithms in the three sequences.

Applied to different resolution images and hardware processing platforms, different algorithms have different runtimes. To better evaluate the real-time performance of different algorithms, the calculation time of each pixel is used as the real-time evaluation indicator on the hardware platform used in this paper.

The t is defined as

$$t = \frac{\text{Detection time of sequence images}}{\text{Total number of pixels in sequence images}} \tag{21}$$

The results are shown in Table 5. It can be seen from Table 5 that ILCM runs the fastest among the former six algorithms, while the proposed algorithm is faster than

Table 5. Time t of different algorithms.

Algorithms	LCM	ILCM	TLWLCM	HWLCM	SWLCM	WSLCM	Proposed
t [µs]	280.963	76.727	195.371	132.198	104.598	386.594	26.224

ILCM. Therefore, the real-time detection performance of the proposed algorithm is much higher than that of the other six algorithms.

5. Conclusion

It is well known that different regions of an image have different grayscale distributions and structural features. In this paper, combining the structure tensor and region complexity, a novel algorithm is proposed to improve the target enhancement and background suppression abilities. The proposed algorithm combines the idea of local contrast to construct the structure tensor matrix, which can better describe the gradient features in the local image area. Then the larger eigenvalue of the matrix is used to weight the corresponding pixel value of the original image. This calculation method can enhance the target more accurately and effectively. Finally, the regional complexity is further introduced to weight the local contrast, which improves the saliency of the target. Compared with other algorithms in SCRG, BSF, ROC curve and detection time comprehensively, the proposed algorithm can achieve a better detection performance for small targets in long-distance airspace.

In our future work, we will focus on improving the operating efficiency of the algorithm. Considering that the proposed algorithm needs to calculate the local contrast of the whole image, we will try to screen out some suspicious areas from the original image, and then calculate the local contrast in the suspicious areas.

Acknowledgements
This work was supported by the National Natural Science Foundation of China (61861033) and the Science Foundation of Nanchang Hongkong University (EA200608037).

References

[1] Du J., Lu H., Zhang L., Hu M., Chen S., Deng Y., *A spatial-temporal feature-based detection framework for infrared dim small target*, IEEE Transactions on Geoscience and Remote Sensing **60**, 2022: 3000412. https://doi.org/10.1109/TGRS.2021.3117131

[2] Wang G., Tao B., Kong X., Peng Z., *Infrared small target detection using nonoverlapping patch spatial–temporal tensor factorization with capped nuclear norm regularization*, IEEE Transactions on Geoscience and Remote Sensing **60**, 2022: 5001417. https://doi.org/10.1109/TGRS.2021.3126608

[3] Wang H., Liu C., Ma C., Ma S., *A novel and high-speed local contrast method for infrared small-target detection*, IEEE Geoscience and Remote Sensing Letters **17**(10), 2020: 1812-1816. https://doi.org/10.1109/LGRS.2019.2951918

[4] Dai Y., Wu Y., Zhou F., Barnard K., *Attentional local contrast networks for infrared small target detection*, IEEE Transactions on Geoscience and Remote Sensing **59**(11), 2021: 9813-9824. https://doi.org/10.1109/TGRS.2020.3044958

[5] Qin Y., Bruzzone L., Gao C., Li B., *Infrared small target detection based on facet kernel and random walker*, IEEE Transactions on Geoscience and Remote Sensing **57**(9), 2019: 7104-7118. https://doi.org/10.1109/TGRS.2019.2911513

[6] Qiu Z., Ma Y., Fan F., Huang J., Wu M., *Adaptive scale patch-based contrast measure for dim and small infrared target detection*, IEEE Geoscience and Remote Sensing Letters **19**, 2022: 7000305. https://doi.org/10.1109/LGRS.2020.3036842

[7] Wang K., Du S., Liu C., Cao Z., *Interior attention-aware network for infrared small target detection*, IEEE Transactions on Geoscience and Remote Sensing **60**, 2022: 5002013. https://doi.org/10.1109/TGRS.2022.3163410

[8] Zhang K., Yang K., Li S., Chen H.-B., *A difference-based local contrast method for infrared small target detection under complex background*, IEEE Access **7**, 2019: 105503-105513. https://doi.org/10.1109/ACCESS.2019.2932729

[9] Han J., Liu S., Qin G., Zhao Q., Zhang H., Li N., *A local contrast method combined with adaptive background estimation for infrared small target detection*, IEEE Geoscience and Remote Sensing Letters **16**(9), 2019: 1442-1446. https://doi.org/10.1109/LGRS.2019.2898893

[10] Zhang P., Zhang L., Wang X., Shen F., Pu T., Fei C., *Edge and corner awareness-based spatial–temporal tensor model for infrared small-target detection*, IEEE Transactions on Geoscience and Remote Sensing **59**(12), 2021: 10708-10724. https://doi.org/10.1109/TGRS.2020.3037938

[11] Sadjadi F.A., *Infrared target detection with probability density functions of wavelet transform subbands*, Applied Optics **43**(2), 2004: 315-323. https://doi.org/10.1364/AO.43.000315

[12] Bai X., Zhou F., *Analysis of new top-hat transformation and the application for infrared dim small target detection*, Pattern Recognition **43**(6), 2010: 2145-2156. https://doi.org/10.1016/j.patcog.2009.12.023

[13] Deshpande S.D., Er M.H., Venkateswarlu R., Chan P., *Max-mean and max-median filters for detection of small targets*, Proceedings of the SPIE, Vol. 3809, Signal and Data Processing of Small Targets 1999: 74-83. https://doi.org/10.1117/12.364049

[14] Pang D., Shan T., Li W., Ma P., Tao R., Ma Y., *Facet derivative-based multidirectional edge awareness and spatial–temporal tensor model for infrared small target detection*, IEEE Transactions on Geoscience and Remote Sensing **60**, 2022: 5001015. https://doi.org/10.1109/TGRS.2021.3098969

[15] Liu T., Yang J., Li B., Xiao C., Sun Y., Wang Y., *Nonconvex tensor low-rank approximation for infrared small target detection*, IEEE Transactions on Geoscience and Remote Sensing **60**, 2022: 5614718. https://doi.org/10.1109/TGRS.2021.3130310

[16] Xiong B., Huang X., Wang M., *Local gradient field feature contrast measure for infrared small target detection*, IEEE Geoscience and Remote Sensing Letters **18**(3), 2021: 553-557. https://doi.org/10.1109/LGRS.2020.2976208

[17] Han J., Liang K., Zhou B., Zhu X., Zhao J., Zhao L., *Infrared small target detection utilizing the multiscale relative local contrast measure*, IEEE Geoscience and Remote Sensing Letters **15**(4), 2018: 612-616. https://doi.org/10.1109/LGRS.2018.2790909

[18] Sun Y., Yang J., An W., *Infrared dim and small target detection via multiple subspace learning and spatial-temporal patch-tensor model*, IEEE Transactions on Geoscience and Remote Sensing **59**(5), 2021: 3737-3752. https://doi.org/10.1109/TGRS.2020.3022069

[19] Han J., Moradi S., Faramarzi I., Liu C., Zhang H., Zhao Q., *A local contrast method for infrared small-target detection utilizing a tri-layer window*, IEEE Geoscience and Remote Sensing Letters **17**(10), 2020: 1822-1826. https://doi.org/10.1109/LGRS.2019.2954578

[20] Yan Z., Xin Y., Zhang Y., *Local contrast measure with iterative error for infrared small target detection*, IET Image Processing **14**(15), 2020: 3725-3732. https://doi.org/10.1049/iet-ipr.2020.1157

[21] Chen C.L.P., Li H., Wei Y., Xia T., Tang Y.Y., *A local contrast method for small infrared target detection*, IEEE Transactions on Geoscience and Remote Sensing **52**(1), 2014: 574-581. https://doi.org/10.1109/TGRS.2013.2242477

[22] Zhang X., Ding Q., Luo H., Hui B., Chang Z., Zhang J., *Infrared dim target detection algorithm based on improved LCM*, Infrared and Laser Engineering **46**(7), 2017: 726002. https://doi.org/10.3788/irla201746.0726002

[23] Du P., Hamdulla A., *Infrared small target detection using homogeneity-weighted local contrast measure*, IEEE Geoscience and Remote Sensing Letters **17**(3), 2020: 514-518. https://doi.org/10.1109/LGRS.2019.2922347

[24] Han J., Moradi S., Faramarzi I., Zhang H., Zhao Q., Zhang X., *Infrared small target detection based on the weighted strengthened local contrast measure*, IEEE Geoscience and Remote Sensing Letters **18**(9), 2021: 1670-1674. https://doi.org/10.1109/LGRS.2020.3004978

[25] Chen Y., Han J., Zhang H., Sang X., *Infrared small dim target detection using local contrast measure weighted by reversed local diversity*, Infrared and Laser Engineering **50**(8), 2021: 20200418. https://doi.org/10.3788/IRLA20200418

[26] Lu R., Yang X., Li W., Fan J., Li D., Jing X., *Robust infrared small target detection via multidirectional derivative-based weighted contrast measure*, IEEE Geoscience and Remote Sensing Letters **19**, 2022: 7000105. https://doi.org/10.1109/LGRS.2020.3026546

[27] Deng H., Sun X., Liu M., Ye C., Zhou X., *Small infrared target detection based on weighted local difference measure*, IEEE Transactions on Geoscience and Remote Sensing **54**(7), 2016: 4204-4214. https://doi.org/10.1109/TGRS.2016.2538295

[28] Dong L., Wang B., Zhao M., Xu W., *Robust infrared maritime target detection based on visual attention and spatiotemporal filtering*, IEEE Transactions on Geoscience and Remote Sensing **55**(5), 2017: 3037-3050. https://doi.org/10.1109/TGRS.2017.2660879

[29] Shi Y., Wei Y., Yao H., Pan D., Xiao G., *High-boost-based multiscale local contrast measure for infrared small target detection*, IEEE Geoscience and Remote Sensing Letters **15**(1), 2018: 33-37. https://doi.org/10.1109/LGRS.2017.2772030

[30] Xia C., Li X., Zhao L., Shu R., *Infrared small target detection based on multiscale local contrast measure using local energy factor*, IEEE Geoscience and Remote Sensing Letters **17**(1), 2020: 157-161. https://doi.org/10.1109/LGRS.2019.2914432

[31] Guan X., Peng Z., Huang S., Chen Y., *Gaussian scale-space enhanced local contrast measure for small infrared target detection*, IEEE Geoscience and Remote Sensing Letters **17**(2), 2020: 327-331. https://doi.org/10.1109/LGRS.2019.2917825

[32] Moradi S., Moallem P., Sabahi M.F., *Scale-space point spread function based framework to boost infrared target detection algorithms*, Infrared Physics & Technology **77**, 2016: 27-34. https://doi.org/10.1016/j.infrared.2016.05.007

[33] Qin Y., Li B., *Effective infrared small target detection utilizing a novel local contrast method*, IEEE Geoscience and Remote Sensing Letters **13**(12), 2016: 1890-1894. https://doi.org/10.1109/LGRS.2016.2616416

[34] Han J., Jiang Y., Zhang X., Liang K., Li Z., Dong X., Li N., *Infrared small target detection using tri-layer window local contrast*, Infrared and Laser Engineering, **50**(2), 2021: 20200146. https://doi.org/10.3788/IRLA20200146

[35] Duan S., Wang Z., Ye Z., *An infrared small object detection algorithm based on spatial weighted local contrast*, Laser and Infrared **50**(10), 2020: 1200-1206.

[36] Zhang C., He Y., Tang Q., Chen Z., Mu T., *Infrared small target detection via interpatch correlation enhancement and joint local visual saliency prior*, IEEE Transactions on Geoscience and Remote Sensing **60**, 2022: 5001314. https://doi.org/10.1109/TGRS.2021.3128189

[37] Bai X., Bi Y., *Derivative entropy-based contrast measure for infrared small-target detection*, IEEE Transactions on Geoscience and Remote Sensing **56**(4), 2018: 2452-2466. https://doi.org/10.1109/TGRS.2017.2781143

Received March 20, 2024
in revised form June 5, 2024